RSC Advances

PAPER

View Article Online
View Journal | View Issue

Cite this: *RSC Adv.*, 2017, **7**, 23793

Synergistic interaction between embedded Co_3O_4 nanowires and graphene papers for high performance capacitor electrodes

Jaeho Choi, Myeongjin Kim and Jooheon Kim *

Received 9th March 2017
Accepted 25th April 2017

DOI: 10.1039/c7ra02867a

rsc.li/rsc-advances

Graphene/Co_3O_4 nanowire composite films were successfully synthesized using a simple, three-step treatment, and the effect of the Co_3O_4 nanowire content on the electrochemical properties of the composite films was studied. The one-dimensional Co_3O_4 nanowires were homogeneously embedded and dispersed between prepared graphene papers, forming a layered graphene/Co_3O_4 nanowire hybrid structure. These composite films exhibited better electrochemical properties than previously reported ones, such as graphene/CNT, where carbon spheres existed in the graphene composites, which were fabricated using the same method but without the Co_3O_4 nanowires. The addition of a small amount of Co_3O_4—typically 8 : 1 by weight (reduced graphene oxide (RGO) : Co_3O_4)—to form thick RGO/Co_3O_4 sandwiches in the form of papers resulted in an excellent specific charge capacity of 278.936 C g^{-1} at a scan rate of 5 mV s^{-1}. These results indicate the potential of the composite for the development of highly capacitive energy storage devices for practical applications.

1. Introduction

It is important to develop sustainable and renewable energy storage systems because of fossil fuel depletion, environmental pollution, and global warming.[1,2] Supercapacitors are among the most promising candidates for this owing to their high power densities and long life cycles. Supercapacitors are emerging as a new class of energy storage devices because they can store more energy than conventional capacitors and provide higher power than batteries.[3] Thus, supercapacitors can be applied to numerous electronic devices, including hybrid electric vehicles, laptops, smartphones, and cameras. However, to satisfy the increasing energy demands of next-generation portable and flexible devices, the energy densities of supercapacitors must be increased significantly without loss of power density or cycle life.[4]

In general, supercapacitors can be classified as electrical double-layer capacitors (EDLCs) or pseudocapacitors according to their charge–discharge mechanisms. EDLCs are charged using a double Helmholtz layer at the interfaces between the electrolyte and the electrodes.[5] The electrodes must have a large surface area, good electronic conductivity, and superior chemical stability. An attractive electrode material for EDLCs is graphene, which satisfies the aforementioned conditions (*e.g.*, providing a large surface area of ~2630 m^2 g^{-1}).[6,7] Thus far, many studies have focused on graphene as an outstanding electrode material for EDLCs; however, the actual capacitance of graphene does not match the expected capacitance. This is because of the coalescence that occurs in the graphene papers during the reduction process, which changes graphene oxide (GO) into graphene.[8] Therefore, researchers commonly use porous electrode materials with a large surface area, such as activated carbon and carbon aerogels, for EDLCs. According to Taberna *et al.*, activated carbon exhibited a specific capacitance of 95 F g^{-1} at a scan rate of 2 mV s^{-1}.[9] In addition, Lee *et al.* reported that carbon aerogels exhibited a specific capacitance of 81 F g^{-1} at a scan rate of 10 mV s^{-1}.[10]

Researchers have examined changes in the structure of EDLC materials, such as the variation of the pore size, which can increase the capacitance and stabilize the rate performance.[11–14] However, these materials were prepared as a slurry with a binder, typically using polyvinylidene fluoride. Some researchers do not use a binder because it connects the active material and the conductive material, inhibiting the capacitance of the EDLC.[15–19] To prevent this, many researchers have embedded a one-dimensional (1D) structure between the graphene papers to increase the surface area of the graphene layer. Huang *et al.* reported the effects of the CNT content on the supercapacitive performance of graphene papers.[20] They introduced different contents of 1D CNT between the graphene papers to increase the contact with the electrolytes. However, the electrical capacitance and the CNT content were not proportional, because CNT—which has a lower capacitance than graphene papers—was the main source of capacitance. Thus, they only had to determine the optimal CNT content. Wang *et al.* investigated a graphene film with intercalated carbon spheres.[21] In both of these studies, an EDLC material was introduced between the graphene papers and was not the

School of Chemical Engineering & Materials Science, Chung-Ang University, Seoul 156-756, Republic of Korea. E-mail: jooheonkim@cau.ac.kr

primary determinant of the specific capacitance. It was used only for widening the gap between the layers. Pseudocapacitive materials such as Fe_3O_4, Co_3O_4, RuO_2, and NiO induce redox reactions, increasing the capacitance and are thus suitable substitutes for EDLC materials.

In this study, the capacitance was increased by embedding a proper quantity of 1D nanowires. In contrast, previous studies involved the introduction of EDLC materials such as CNT and MnO_2 particles. Metal oxides such as Co_3O_4, NiO, and RuO_2 have a superior capacitance compared to carbon materials.[22–24] Therefore, we embedded 1D Co_3O_4 nanowires between graphene papers. Several reduced GO (RGO)/Co_3O_4 nanowire composites have been obtained from GO/Co_3O_4 *via* thermal reduction at high temperatures. In these composites, the Co_3O_4 nanowires increase the specific surface area and the reversible pseudocapacitance and decrease the diffusion path. Graphene papers serve primarily as highly conductive supports and can provide large surface areas for the deposition of nanoscale Co_3O_4. The morphologies and microstructural characteristics of the RGO/Co_3O_4 nanocomposites were investigated in detail. The specific capacitance of each Co_3O_4-containing sample were also investigated, at a scan rate of 5 mV s^{-1}. In addition to electrochemical characterization, such as galvanostatic charge/discharge (GCD) measurements, electrochemical impedance spectroscopy (EIS) was performed. These results suggest the great potential of the composite for the development of highly capacitive energy-storage devices for practical applications.

2. Experimental

2.1. Preparation of GO papers

GO papers were synthesized using the modified Hummers method. All reagents were used without further purification.[25] Three grams of graphite powder (graphene supermarket) was added to a mixture containing 40 mL of concentrated phosphoric acid (85% Daejung Chemical Co., Korea) and 360 mL of concentrated sulfuric acid (95% Daejung Chemical Co., Korea). The resulting mixture was stirred in an ice bath for 4 h until the graphite powder was homogeneously dispersed. Then, 18 g of $KMnO_4$ (≥99% Sigma-Aldrich) was slowly added to the solution in an ice bath over 1 h at 0 °C. The resulting mixture was stirred in an oil bath at 50 °C for 12 h. It was then poured into 400 mL of deionized (DI) water (resistivity > 18.3 Mohm cm^{-1}) with 3 mL of H_2O_2 (30% Daejung Chemical Co., Korea), and the resulting mixture was stirred for 4 h. Next, the mixture was centrifuged and washed with HCl (20% Daejung Chemical Co., Korea) and DI water several times. After centrifugation to remove the supernatant and re-dispersion, the graphite oxide was collected and then dispersed in DI water *via* ultrasonication to exfoliate it into GO papers. The resulting product was dried in a vacuum oven at 50 °C for 48 h, yielding GO particles with an average length of several micrometers and thickness of 4–5 nm.

2.2. Preparation of Co_3O_4 nanowires

All of the chemicals were analytical-grade and were used without further purification. The experimental details were as follows. First, 2.5 g of cetyltrimethylammonium bromide (CTAB) (Sigma-Aldrich) was dissolved in a mixture of 75 mL of cyclohexane (99.5% Sigma-Aldrich) and 2.5 mL of *n*-amyl alcohol (≥99% Sigma-Aldrich). After 20 min of stirring, 3.75 mL of aqueous 0.1 M $H_2C_2O_4$ (≥99% Sigma-Aldrich) was added to the CTAB solution, and the resulting mixture was stirred for an additional 25 min. Finally, 1.25 mL of 0.1 M $CoSO_4 \cdot 7H_2O$ (≥99% Sigma-Aldrich) was added to the resulting microemulsion, and the mixture was stirred for 24 h at room temperature. After the reaction was complete, the products were centrifuged, washed with DI water and ethanol to remove any remaining ions, and dried at 80 °C in air. The resulting powders were annealed at 550 °C for 4 h in air.

2.3. Preparation of graphene/Co_3O_4 layered film

Hybrid composite structures were prepared *via* solvent mixing and filtration. In the first step, 0.05 g of GO was suspended with various proportions of Co_3O_4 nanowires (graphene : Co_3O_4 nanowire ratios of 10 : 1, 8 : 1, 5 : 1, and 3 : 1 by weight) in 20 mL of tetrahydrofuran. The resulting mixtures, denoted as GO/Co_3O_4 10 : 1, GO/Co_3O_4 8 : 1, GO/Co_3O_4 5 : 1, and GO/Co_3O_4 3 : 1, respectively, were ultrasonicated for 3 h, filtered through a 0.2 μm-SiO_2 membrane (Anodisc, Whatman, USA) and washed with DI water several times. After filtration, the resulting product was subjected to reduction *via* annealing at 300 °C for 1 h in N_2. The final products are denoted as RGO/Co_3O_4 10 : 1, RGO/Co_3O_4 8 : 1, RGO/Co_3O_4 5 : 1 and RGO/Co_3O_4 3 : 1, respectively.

2.4. Characterization methods

The X-ray diffraction (XRD) patterns were collected (New D8-Advance/Bruker-AXS) at a scan rate of 1° s^{-1} with a 2θ range of 5–80° and Fe Kα1 radiation (0.1793 nm). Field-emission scanning electron microscopy (FE-SEM, SIGMA, Carl Zeiss) was performed to examine the morphologies of graphene, Co_3O_4, and the graphene composite samples. The compositions of the samples were investigated *via* thermogravimetric analysis (TGA, TA Instruments TGA-2050) at a heating rate of 20 °C min^{-1} in flowing N_2. Raman spectra were recorded on a Raman Station 400F (Perkin-Elmer), using a near infrared laser operating at 758 nm with a CCD detector. X-ray photoelectron spectroscopy (XPS, Thermo U.K. K-Alpha) with a monochromatic Al Kα X-ray source (1486.6 eV) was performed to investigate the binding energies of the materials.

2.5. Preparation and characterization of supercapacitors

A three-electrode cell was used to perform electrochemical tests. A Ag/AgCl (KCl-saturated) electrode and platinum foil were used as the reference and counter electrodes, respectively. The papers were pressed (4000 psi) onto nickel foam current collectors, which were used as the working electrode. The measurements were performed in a 2 M aqueous KOH electrolyte at room temperature. Cyclic voltammetry (CV), GCD characterization, and EIS were performed using a CHI 660C electrochemical workstation. The EIS measurements were performed using an alternating-current voltage with an amplitude of 5 mV in the frequency range 10^5 to 0.1 Hz and an open-circuit potential.

3. Results and discussion

Scheme 1 illustrates the entire procedure for preparing Co_3O_4 nanowire-embedded graphene paper (RGO/Co_3O_4), which consists of the following three steps: (i) the syntheses of the GO suspension and the Co_3O_4 nanowire by the modified Hummers method and the calcination of CoC_2O_4 nanowires, respectively; (ii) the fabrication of sheet-type hybrid Co_3O_4 nanowire-embedded GO paper (GO/Co_3O_4) by filtration of the Co_3O_4 nanowire-added GO solution mixture; and (iii) the reduction of GO/Co_3O_4 to Co_3O_4 nanowire-embedded graphene paper (RGO/Co_3O_4) by thermal treatment. The morphologies and detailed structures of the GO paper, Co_3O_4 nanowires, and GO/Co_3O_4 8 : 1 paper were characterized using FE-SEM. Fig. 1(a) shows a cross-sectional image of the as-synthesized GO paper, which indicates compact stacking between the GO layers. Fig. 1(b) shows pure Co_3O_4 nanowires, which were predominantly cylindrical and had average lengths and diameters of ~1 and ~15 nm, respectively. A cross-sectional FE-SEM image of the GO/Co_3O_4 8 : 1 paper taken after the filtration of the Co_3O_4 nanowire-added GO solution mixture (weight ratio of RGO : Co_3O_4 was 8 : 1) indicates that the Co_3O_4 nanowires were successfully embedded between the GO layers (Fig. 1(c)). Fig. 1(d) shows the representative XRD patterns of the GO paper, Co_3O_4 nanowires, and GO/Co_3O_4 8 : 1 paper. The XRD pattern of GO reveals that the highest-intensity peak of GO at $2\theta = 11.5^\circ$—corresponding to the (0 0 1) reflection—and the interlayer spacing were substantially larger than those of pristine graphite owing to the introduction of oxygen-containing functional groups on the graphite sheets. Five obvious diffraction peaks at 2.969, 2.495, 2.023, 1.556 and 1.435 Å in the XRD patterns can be assigned to the (2 2 0), (3 1 1), (4 0 0), (5 1 1) and (4 4 0) reflections of the crystal planes. These assigned patterns were observed at $2\theta = 30.1^\circ$, 36°, 44.8°, 59.4°, and 65°, respectively. No diffraction peaks from species other than Co_3O_4 are observed, indicating the high purity of the synthesized product.

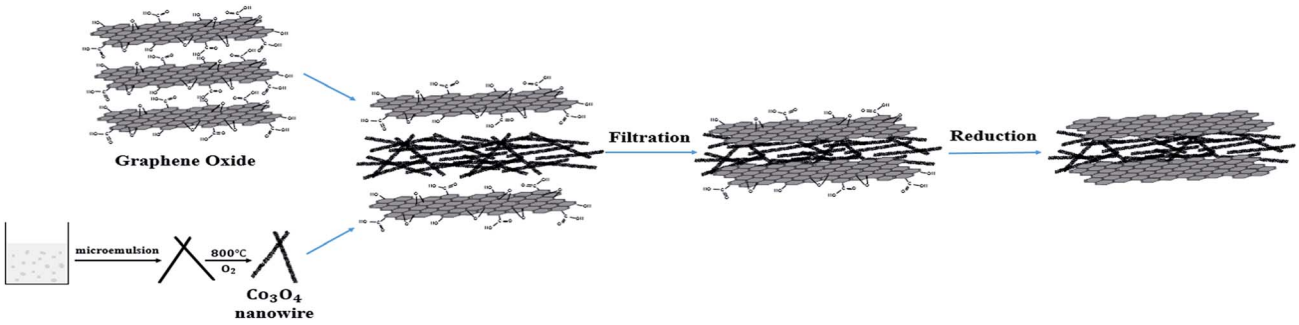

Scheme 1 Schematic illustration of synthesis of RGO/Co_3O_4 electrode.

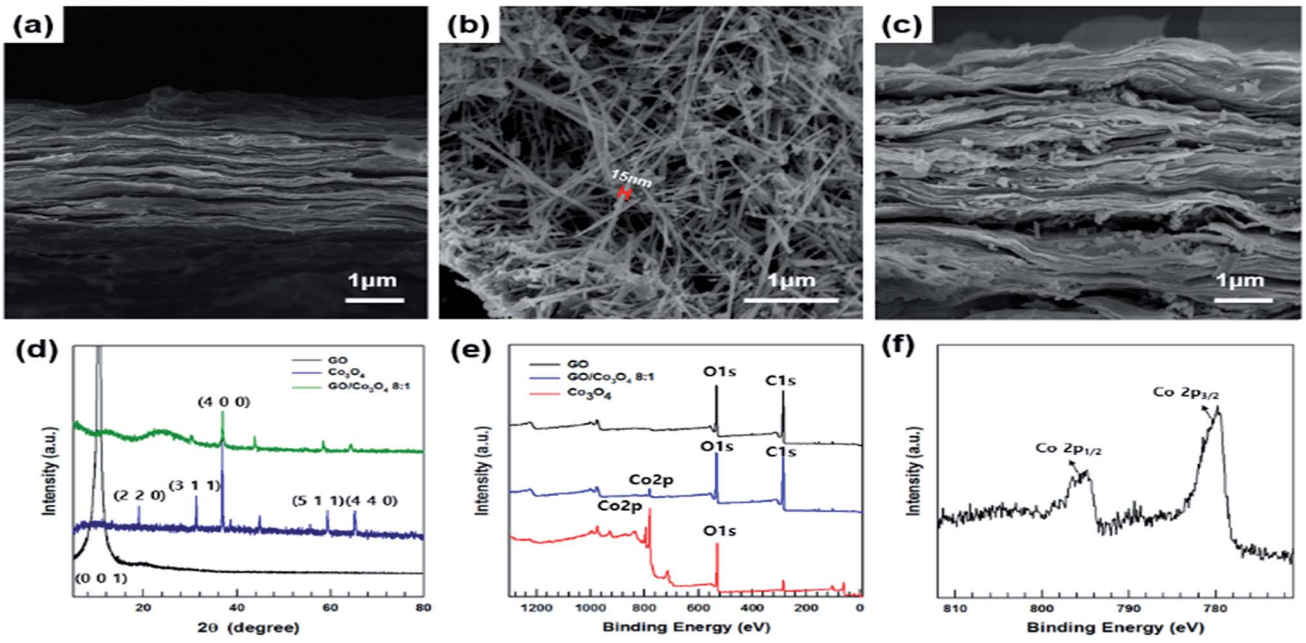

Fig. 1 FE-SEM cross section image of (a) pristine GO paper, (b) Co_3O_4 nanowires, (c) GO/Co_3O_4 8 : 1, (d) XRD patterns of pristine GO, Co_3O_4 nanowire, GO/Co_3O_4 8 : 1, (e) XPS wide scan spectra of pristine GO, Co_3O_4 nanowire, GO/Co_3O_4 8 : 1, (f) Co 2p scan spectra of GO/Co_3O_4 8 : 1.

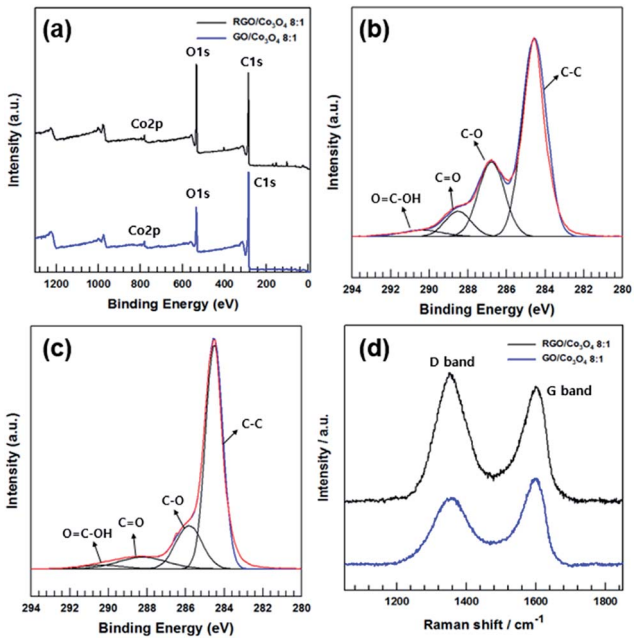

Fig. 2 XPS (a) wide scan spectra of GO/Co_3O_4 8 : 1 and RGO/Co_3O_4 8 : 1 (b) C 1s scan spectra of GO/Co_3O_4 8 : 1 (c) C 1s scan spectra of RGO/Co_3O_4 8 : 1 (d) Raman spectra of GO/Co_3O_4 8 : 1 and RGO/Co_3O_4 8 : 1.

After the intercalation of the Co_3O_4 nanowires between the GO layers, the XRD pattern of the synthesized GO/Co_3O_4 8 : 1 paper exhibited both GO and Co_3O_4 diffraction peaks, indicating that the Co_3O_4 nanowires were successfully embedded between the GO layers. The XPS wide-scan spectra of the GO paper, Co_3O_4 nanowires, and GO/Co_3O_4 8 : 1 paper are shown in Fig. 1(e). The XPS survey spectrum of the GO paper comprises only two elements: carbon and oxygen. However, a cobalt signal (Co 2p) emerged in the XPS spectra of the GO/Co_3O_4 8 : 1 paper, indicating that the Co_3O_4 nanowires were well-embedded between the GO layers. To obtain more detailed surface information, the XPS Co 2p core-level spectra of the GO/Co_3O_4 8 : 1 paper was deconvoluted. The resulting Co 2p spectrum has two peaks at binding energies of 780 and 795.1 eV, corresponding to Co $2p_{3/2}$ and Co $2p_{1/2}$, respectively (Fig. 1(e)).

To fabricate the supercapacitor electrodes, the GO/Co_3O_4 paper was reduced to RGO/Co_3O_4 paper *via* thermal treatment. Fig. 2(a) shows the XPS wide-scan spectra of the GO/Co_3O_4 and RGO/Co_3O_4 papers. After the reduction of the GO/Co_3O_4 paper, the intensity of the O 1s peak was dramatically decreased, indicating the removal of oxygen-containing functional groups *via* thermal treatment. Fig. 2(b) and (c) show the deconvoluted C 1s core-level spectra of the GO/Co_3O_4 and RGO/Co_3O_4 papers, respectively. Table 1 summarizes the differences in the elemental compositions of the GO/Co_3O_4 and RGO/Co_3O_4 papers. The C 1s spectra of GO/Co_3O_4 (Fig. 2(b)) show strong binding-energy peaks of aromatic C–C/C=C and C–O/C–O–C bonds at 284.5 and 286.5 eV, respectively, with several binding-energy peaks of functional groups containing oxygen, such as C=O at 288.1 eV and O=C–OH at 289.0 eV. Compared with the case of GO/Co_3O_4, in the C 1s spectrum of RGO/Co_3O_4 (Fig. 2(c)), the area of the peak associated with C–C/C=C became predominant, whereas the area corresponding to C–O, C=O, and O=C–OH decreased dramatically. The heterocarbon component of RGO/Co_3O_4 (30.4 at%) decreased to a greater extent than that of GO/Co_3O_4 (66.8 at%), indicating the successful reduction of GO/Co_3O_4. To further investigate the reduction effect, Raman spectroscopy was performed, and the results are shown in Fig. 2(d). In the case of GO/Co_3O_4, the typical features in the Raman spectra are the G band at 1585 cm^{-1} and the D band at 1335 cm^{-1}. The G band is characteristic of sp^2-hybridized C–C bonds in a two-dimensional hexagonal lattice, and the D band corresponds to the defects and disordered carbon in the graphite layers. After being reduced by thermal treatment, the D-band peak intensity of RGO/Co_3O_4 was increased dramatically, and the RGO/Co_3O_4 exhibited a far higher intensity ratio of the D band to the G band (I_D/I_G: 0.95) than that of GO/Co_3O_4 (I_D/I_G: 0.88) owing to the increase in the number of defects due to the removal of oxygen-containing functional groups.

To investigate the differences between RGO/Co_3O_4 papers made using different Co_3O_4 feeding ratios, the XPS wide-scan spectra of RGO/Co_3O_4 10 : 1, RGO/Co_3O_4 8 : 1, RGO/Co_3O_4 5 : 1, and RGO/Co_3O_4 3 : 1 were measured, as shown in Fig. 3(a). The Co 2p and O 1s peaks exhibit a gradual increase in intensity with increasing Co_3O_4 feeding ratios in the RGO/Co_3O_4 papers. To further examine the Co_3O_4 content in the RGO/Co_3O_4 papers, TGA was performed, and the results are shown in Fig. 3(b). The experiments were performed up to 800 °C in air, with a heating rate of 20 °C min^{-1}. Under these conditions, the RGO paper began to lose weight below 100 °C, which is attributed to the dehydration of physisorbed water. Weight loss in the second step at ~190 °C was caused by the evolution of CO and CO_2 due to the removal of oxygen-containing groups from the surface of the RGO. The weight loss at ~440 °C is attributed to the combustion of the carbon skeleton of the RGO. Finally, the RGO was completely removed at ~700 °C.[26] Pure Co_3O_4 nanowires exhibited negligible weight loss until 800 °C. The weight-loss values for Co_3O_4, RGO/Co_3O_4 10 : 1, RGO/Co_3O_4 8 : 1, RGO/Co_3O_4 5 : 1, RGO/Co_3O_4 3 : 1, and RGO were 0.15, 91.29, 88.22, 83.10, 73.42, and 99.44 wt%, respectively. These results agree well with the XPS analysis (Fig. 3(a)). Fig. 3(c) shows the XRD patterns of RGO and RGO/Co_3O_4 papers. The XRD pattern of the RGO paper exhibits a significant diffraction peak at $2\theta = 24.5°$, which is attributed to the (0 0 2) reflection of graphitic carbon.[27]

Table 1 The C 1s peak position and the relative atomic percentage of various functional groups in Go/Co_3O_4 8 : 1 and RGO/Co_3O_4 8 : 1

	Fitting of the C 1s peak binding energy [eV] (relative atomic percentage [%])			
	C–C/C=C	C–O/C–O–C	C=O	O=C–OH
GO/Co_3O_4 8 : 1	284.5 (33.2)	286.5 (43.8)	288.1 (15.2)	289.0 (7.8)
RGO/Co_3O_4 8 : 1	284.5 (69.6)	286.4 (16.4)	287.9 (8.4)	289.1 (5.6)

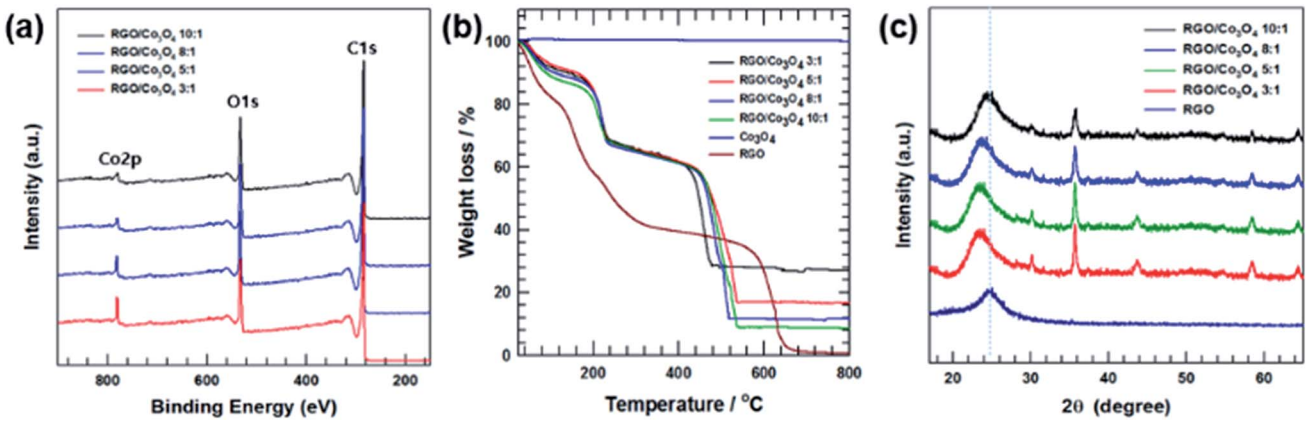

Fig. 3 (a) XPS wide scan spectra of RGO/Co_3O_4 3 : 1, RGO/Co_3O_4 5 : 1, RGO/Co_3O_4 8 : 1 and RGO/Co_3O_4 10 : 1, (b) TGA thermograms of RGO/Co_3O_4 3 : 1, RGO/Co_3O_4 5 : 1, RGO/Co_3O_4 8 : 1, RGO/Co_3O_4 10 : 1, pristine Co_3O_4 and pristine RGO, (c) XRD patterns of RGO/Co_3O_4 10 : 1, RGO/Co_3O_4 8 : 1, RGO/Co_3O_4 5 : 1, RGO/Co_3O_4 3 : 1 and pristine RGO.

The RGO/Co_3O_4 papers exhibit several obvious diffraction peaks, which are assigned to the (2 2 0), (3 1 1), (4 0 0), (5 1 1), and (4 4 0) planes in the standard Co_3O_4 spectrum.[28] With the increase of the Co_3O_4 feeding ratio, the XRD diffraction peaks associated with Co_3O_4 gradually increased in intensity, exhibiting the same trend as the XPS results (Fig. 3(a)). Importantly, as the feeding ratio of RGO : Co_3O_4 increased to 5 : 1, the 2θ value of the (0 0 2) plane was gradually reduced, indicating that the *d*-spacing of the graphene layer increased owing to the intercalation of Co_3O_4 nanowires. However, when the feeding ratio was higher than 5 : 1, there was no significant change in the 2θ angle of the (0 0 2) plane. These differences in the interlayer distance between the graphene layers, which depend on the Co_3O_4 contents in the RGO/Co_3O_4 papers, likely lead to significant differences in the ion diffusion/transport behavior during the charging/discharging process, affecting the electrochemical performance.

The cross-sectional morphology and structure for the RGO and RGO/Co_3O_4 papers were examined using FE-SEM, as shown in Fig. 4. The cross-sectional FE-SEM image of the RGO paper in Fig. 4(a) shows a compactly packed graphene layer structure. The graphene papers are tightly packed, which hinders the electrolyte diffusion and is unsuitable for supercapacitors. However, in the RGO/Co_3O_4 papers, the interlayer space between the graphene nanosheets due to the Co_3O_4 nanowires is clearly observed. The embedded Co_3O_4 nanowires provide the electrolyte ions increased access to the inside of the electrochemical active materials, which is difficult to achieve in closely packed RGO paper. Therefore, the role of the Co_3O_4 nanowires is not only to physically separate the graphene layers, which form a well-defined sandwich structure, but also to participate in the redox reaction during the charge/discharge process. Cross-sectional FE-SEM images of different amounts of Co_3O_4 nanowires embedded between the graphene layers for the RGO/Co_3O_4 papers are shown in Fig. 4(b)–(e).

To investigate the potential applications for supercapacitors, samples were fabricated into supercapacitor electrodes and characterized *via* CV and GCD measurements. Pure Co_3O_4 nanowires, an RGO film, and RGO/Co_3O_4 10 : 1 electrodes were investigated to obtain clear evidence of the roles of the RGO film and the Co_3O_4 nanowires during the charge/discharge process and the effect of the intercalation of the Co_3O_4 nanowires between the RGO layers. Fig. 5(a) shows CV curves of Co_3O_4, RGO, and RGO/Co_3O_4 10 : 1 electrodes acquired at a scan rate of 5 mV s^{-1} over a potential window of −0.2 to 0.6 V (*vs.* Ag/AgCl) in a 2 M KOH electrolyte. The CV curve of the RGO electrode is almost rectangular, whereas the pure Co_3O_4 electrode exhibits a pair of redox peaks during both the cathodic and anodic processes around 0.34–0.45 V, corresponding to the reversible reactions of $Co^{3+} \leftrightarrow Co^{2+}$ with OH^- ions. These behaviors indicate that the capacitance of the RGO electrode arose mainly from the electric double-layer mechanism, whereas that of the Co_3O_4 electrode arose mainly from faradic mechanisms. The redox peaks of the Co_3O_4 electrode are attributed to the following redox reactions:[29]

$$\begin{aligned} Co(II)_2 + OH^- &\leftrightarrow Co(II)(OH)_{ad} + e^- Co(II)(OH)_{ad} \\ &\leftrightarrow Co(III)(OH)_{ad} + e^- \end{aligned} \quad (1)$$

$$\begin{aligned} Co(III) + OH^- &\leftrightarrow Co(III)(OH)_{ad} + e^- Co(III)(OH)_{ad} \\ &\leftrightarrow Co(IV)(OH)_{ad} + e^- \end{aligned} \quad (2)$$

Interestingly, the shape of the CV curve for the RGO/Co_3O_4 10 : 1 electrode indicates both electric double-layer and faradic reactions. The redox peaks of the RGO/Co_3O_4 10 : 1 electrode are attributed to the redox reaction of the newly intercalated Co_3O_4 nanowires between the RGO layers. A partial contribution from the electric double-layer mechanism is evidenced by the rectangular area around the potential switching regions.

Fig. 5(b) shows the GCD curves of Co_3O_4, RGO, and RGO/Co_3O_4 10 : 1 electrodes acquired at a current density of 0.5 A g^{-1} over a potential window of −0.2 to 0.6 V (*vs.* Ag/AgCl) in the 2 M KOH electrolyte. The charge/discharge curve of the RGO electrode shows a typical triangular shape with a good linear relationship between the charge/discharge potentials and time,

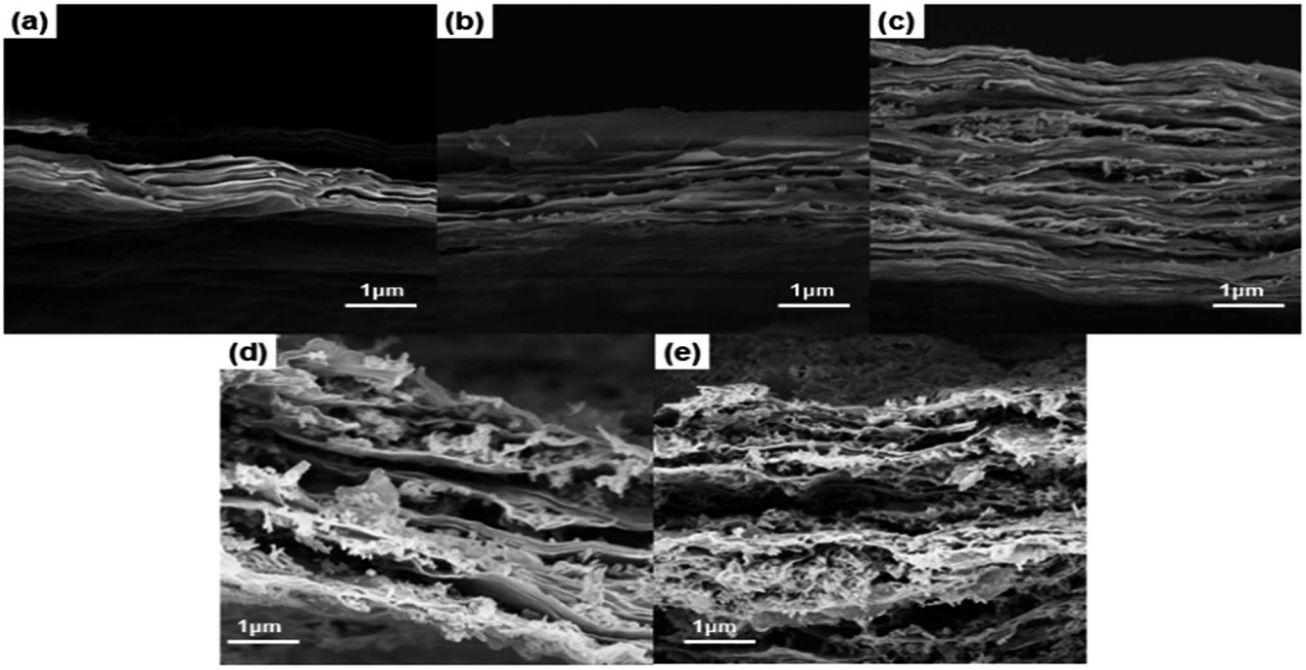

Fig. 4 FE-SEM cross section images of (a) pristine RGO, (b) RGO/Co_3O_4 10 : 1, (c) RGO/Co_3O_4 8 : 1, (d) RGO/Co_3O_4 5 : 1, (e) RGO/Co_3O_4 3 : 1.

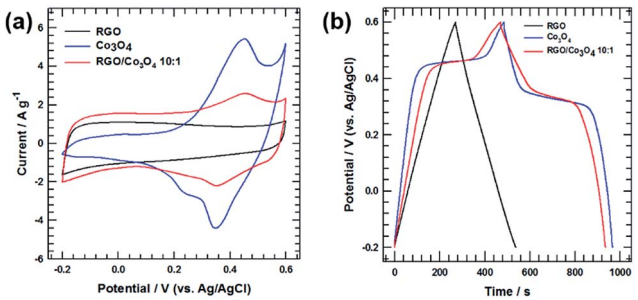

Fig. 5 (a) CV curves of pristine RGO, pristine Co_3O_4, RGO/Co_3O_4 10 : 1 electrodes measured at a scan rate 5 mV s^{-1}. (b) Galvanostatic charge–discharge curves of pristine RGO, pristine Co_3O_4, RGO/Co_3O_4 10 : 1 electrodes measured at a current density of 0.5 A g^{-1}.

which is a typical electric double-layer characteristic. However, the charge/discharge curve for the pure Co_3O_4 electrode has a nonlinear voltage profile with plateau regions around 0.45 V in the charging step and 0.33 V in the discharging step. These correspond to the oxidation and reduction of the Co_3O_4 nanowires. The plateaus well match the redox peak potentials observed in the CV curve. Importantly, the charge/discharge curve for the RGO/Co_3O_4 10 : 1 electrode exhibits both a plateau arising from the faradic reactions of the Co_3O_4 nanowires and a triangular region arising from the electric double-layer capacitive effect of RGO. The specific stored charge capacity (Q, C g^{-1}) is calculated instead of the specific capacitance using the following equation:[30]

$$Q = \left(\int I(V) \mathrm{d}V \right) \Big/ 2vM \quad (3)$$

where Q, $I(v)$, dV, v, and M represent the specific stored charge capacity, the current at V, the differential potential, the scan rate, and the mass of active materials, respectively. The calculated specific stored charge capacities for the RGO, Co_3O_4, and RGO/Co_3O_4 10 : 1 electrodes were 131.392, 238.088, and 230.176 C g^{-1}, respectively, at a scan rate of 5 mV s^{-1}. The improved stored charge capacity of RGO/Co_3O_4 10 : 1 electrode is attributed to the harmonious synergistic effect of the electric capacitive contribution of the RGO film and the faradic reactions of the Co_3O_4 nanowires. In addition, the intercalated Co_3O_4 nanowires between the RGO layers increased the interplanar distances of the (0 0 2) plane of the RGO film, resulting in favorable ion diffusion/transport into the RGO/Co_3O_4 10 : 1 electrode.

To investigate the effects of the Co_3O_4 nanowire content on the electrochemical performance of the RGO/Co_3O_4 films, RGO/Co_3O_4 films were fabricated with various Co_3O_4 feeding ratios. Fig. 6(a) shows the CV curves for RGO/Co_3O_4 10 : 1, RGO/Co_3O_4 8 : 1, RGO/Co_3O_4 5 : 1, and RGO/Co_3O_4 3 : 1 electrodes at a scan rate of 5 mV s^{-1} in a potential window of −0.2 to 0.6 V (*vs.* Ag/AgCl) in the 2 M KOH electrolyte. Importantly, all the RGO/Co_3O_4 electrodes exhibited cathodic and anodic humps during the charge/discharge process, owing to the redox reactions of the Co_3O_4 nanowires, as described by eqn (1) and (2). Based on these discharge times, the specific capacitances of the electrodes were calculated using the following equation:[31]

$$C_s = (I \times t)/(m \times \Delta V) \quad (4)$$

where I is the discharge current, t is the discharge time, m is the mass of active material and ΔV is the voltage drop upon discharge. The calculated specific stored charge capacities for

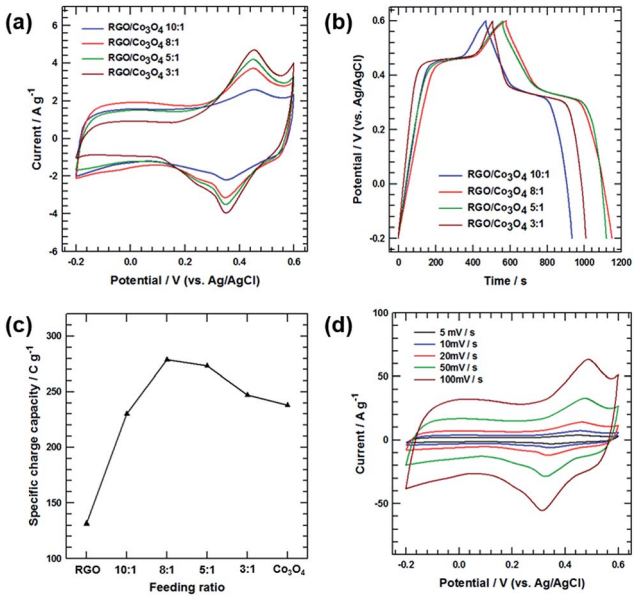

Fig. 6 (a) CV curves of RGO/Co_3O_4 10 : 1, RGO/Co_3O_4 8 : 1, RGO/Co_3O_4 5 : 1 and RGO/Co_3O_4 3 : 1 electrodes measured at a scan rate 5 mV s^{-1}. (b) Galvanostatic charge–discharge curves of RGO/Co_3O_4 10 : 1, RGO/Co_3O_4 8 : 1, RGO/Co_3O_4 5 : 1 and RGO/Co_3O_4 3 : 1 electrodes measured at a current density of 0.5 A g^{-1}. (c) Specific charge capacity of RGO/Co_3O_4 8 : 1 electrode with Co_3O_4 feeding ratio at 5 mV s^{-1}. (d) CV curves of RGO/Co_3O_4 8 : 1 electrode at different scan rates of 5, 10, 20, 50 and 100 mV s^{-1}.

the RGO/Co_3O_4 10 : 1, RGO/Co_3O_4 8 : 1, RGO/Co_3O_4 5 : 1, and RGO/Co_3O_4 3 : 1 electrodes were 230.176, 278.936, 273.176 and 247.016 C g^{-1}, respectively, at a scan rate of 5 mV s^{-1}. The redox peaks of the CV curves became more pronounced as the Co_3O_4 feeding ratio increased, indicating that vigorous redox reactions occurred because the large amount of Co_3O_4 nanowires participated in the redox reaction. Fig. 6(b) shows the GCD curves of the RGO/Co_3O_4 10 : 1, RGO/Co_3O_4 8 : 1, RGO/Co_3O_4 5 : 1, and RGO/Co_3O_4 3 : 1 electrodes acquired at a current density of 0.5 A g^{-1} in a potential window of −0.2 to 0.6 V (*vs.* Ag/AgCl). Notably, all the RGO/Co_3O_4 electrodes exhibited plateau regions at the redox peak potentials observed in the CV curve in both the charging and discharging steps, owing to the reversible redox reactions of Co_3O_4. Moreover, with increasing Co_3O_4 content, the plateau regions observed during charging (at 0.45 V) and discharging (at 0.33 V) were gradually broadened, which agrees well with the CV curves.

Fig. 6(c) shows the specific stored charge capacity with respect to the Co_3O_4 feeding ratio, obtained from the CV curves at a scan rate of 5 mV s^{-1}. In Fig. 6(c), as the feeding ratio of RGO : Co_3O_4 increased from 10 : 1 to 8 : 1, the specific stored charge capacities for the RGO/Co_3O_4 electrodes steadily increased because of the intercalation of a sufficient amount of Co_3O_4 between the RGO layers. The intercalated Co_3O_4 nanowires not only participated in the redox reaction during the charge/discharge process but also facilitated fast and favorable electrolyte ion diffusion/transport by increasing the *d*-spacing of the (0 0 2) plane of the RGO film. However, when the feeding ratio exceeded 8 : 1, the specific stored charge capacity of the RGO/Co_3O_4 5 : 1 and RGO/Co_3O_4 3 : 1 electrodes decreased significantly owing to the diminished electric double-layer contribution of the RGO. Although a large amount of Co_3O_4 nanowires caused a vigorous redox reaction, the Co_3O_4 nanowires were aggregated, providing high-resistance pathways for ion diffusion into the inner space of the RGO/Co_3O_4 film. This hindered the optimization of the electric double layer and the enhancement of the capacitance value, reducing the total capacitive performance. These behaviors are confirmed by the CV curves. As shown in Fig. 6(a), the cathodic and anodic peaks are more pronounced in the case of the RGO/Co_3O_4 5 : 1 and RGO/Co_3O_4 3 : 1 electrodes, indicating that vigorous redox reactions occurred because of the large amount of Co_3O_4 nanowires. However, the shape of the switching-potential regions gradually changed from a rectangle to an oval with decreasing integrated area as function of the increasing Co_3O_4 nanowire content, suggesting a weakened electric double-layer capacitive contribution. To further investigate the rapid charge/discharge characteristics, the RGO/Co_3O_4 8 : 1 electrode was subjected to more detailed measurements. Fig. 6(d) shows the CV curves of the RGO/Co_3O_4 8 : 1 electrode acquired at various scan rates from 5 to 100 mV s^{-1}. The oxidation and reduction peaks shifted negatively and positively as the scan rate increased, depending on the electrical polarization in the electrode. However, the peak position shifted slightly even at high scan rates, indicating the relatively low resistance of the electrode caused by the excellent electrical conductivity of the RGO film.

Fig. 7(a) shows the specific stored charge capacity with respect to the scan rate for RGO, RGO/Co_3O_4 10 : 1, RGO/Co_3O_4 8 : 1, RGO/Co_3O_4 5 : 1, and RGO/Co_3O_4 3 : 1 electrodes. The RGO/Co_3O_4 8 : 1 electrode exhibited the highest capacity over the range of scan rates. The specific stored charge capacity values for all the electrodes steadily decreased as the scan rate increased, owing to the reduced access of the electrolyte ions to the active surface, especially for relatively slow faradic reactions. When the scan rate increased from 5 to 500 mV s^{-1}, the rate performances of the RGO, RGO/Co_3O_4 10 : 1, RGO/Co_3O_4 8 : 1, RGO/Co_3O_4 5 : 1, and RGO/Co_3O_4 3 : 1 electrodes were 78.39%, 84.67%, 80.05%, 76.02%, and 71.68%, respectively. The capacity-retention ratio for the RGO/Co_3O_4 10 : 1 electrode was significantly improved compared with that of the RGO electrode owing to the increased *d*-spacing of (0 0 2) plane of the RGO film caused by the intercalation of the Co_3O_4 nanowires between the RGO layers. The increased interplanar distances of the (0 0 2) plane allowed fast ion diffusion/transport, resulting in fast charge/discharge. However, when the feeding ratio exceeded 10 : 1, the capacity-retention ratios for the RGO/Co_3O_4 electrodes steadily decreased because of the aggregation of the embedded Co_3O_4 nanowires. The aggregated Co_3O_4 nanowires hindered the migration of electrolyte ions into the inner space of the RGO/Co_3O_4 film. These hindrances created high-resistance pathways for ion diffusion, leading to slow ion transport, especially at high scan rates or current densities. If the electrode materials have an ideal structure for low-resistance pathways and fast ion transport, the electric

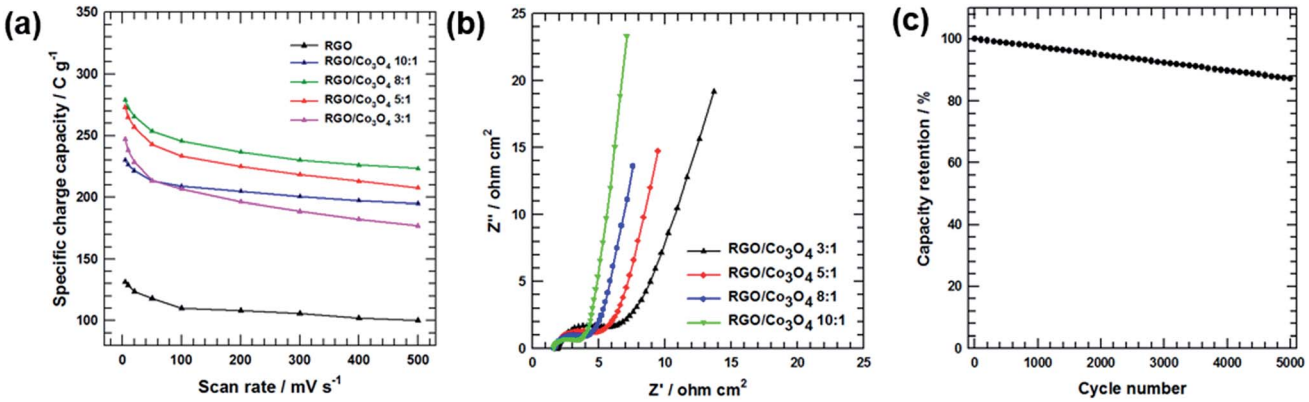

Fig. 7 (a) Specific charge capacity of RGO, RGO/Co_3O_4 10 : 1, RGO/Co_3O_4 8 : 1, RGO/Co_3O_4 5 : 1 and RGO/Co_3O_4 3 : 1 electrodes at different scan rates of 5, 10, 20, 50, 100, 200, 300, 400 and 500 mV s^{-1} (b) Nyquist plots of the RGO, RGO/Co_3O_4 10 : 1, RGO/Co_3O_4 8 : 1, RGO/Co_3O_4 5 : 1 and RGO/Co_3O_4 3 : 1 electrodes, (c) cyclic stability of the RGO/Co_3O_4 8 : 1 measured at 5 mV s^{-1}.

double-layer can be rapidly reorganized at the switching potentials, and the current response can quickly reach a steady state. However, the CV profiles of the RGO/Co_3O_4 electrodes having large amounts of Co_3O_4 (RGO/Co_3O_4 5 : 1 and RGO/Co_3O_4 3 : 1 in Fig. 6(a)) exhibit obvious delays in the current reaching a steady-state value after the reversal of the potential sweep because of the unfavorable ion transfer/diffusion behavior. To investigate the reason for this, EIS was performed on the RGO/Co_3O_4 10 : 1, RGO/Co_3O_4 8 : 1, RGO/Co_3O_4 5 : 1, and RGO/Co_3O_4 3 : 1 electrodes, and the results are shown in Fig. 7(b). The EIS data were analyzed *via* Nyquist plots, which consist of three parts: (i) a semicircle in the high-to-medium frequency region, with its starting cross-point at the Z' axis, indicating the combined series resistance of the electrolyte and the current collectors, along with the electrode/current collector contact resistance (diameter of the semicircle represents the charge-transfer resistance, R_{ct}); (ii) a straight line with a slope of 45° in the low-frequency range, corresponding to the semi-infinite Warburg impedance resulting from the frequency dependence of the ion diffusion/transport in the electrolyte; and (iii) a vertical line at very low frequencies. The nearly vertical line indicates good capacitive behavior without diffusion limitations.[32] All the RGO/Co_3O_4 electrodes exhibited semicircles in the high-to-medium frequency region due to the faradaic reactions of the Co_3O_4 nanowires. Importantly, the diameter of the semicircle in the high-frequency range and the slope of vertical line in the low-frequency range differ significantly according to the Co_3O_4 content. When the Co_3O_4 content was increased, vigorous faradic reactions occurred more readily, causing the gradual increase of the charge-transfer resistance. Moreover, the slope of the vertical line in the low-frequency region gradually decreased as the Co_3O_4 content increased, indicating the presence of high-resistance pathways for ion diffusion into the inner space of the RGO/Co_3O_4 film. Therefore, the trend of the vertical-line slope for the RGO/Co_3O_4 electrodes agrees with the rate-capability performance obtained from the CV measurements (Fig. 7(a)). Fig. 7(c) shows the cycling stability of the RGO/Co_3O_4 8 : 1 electrode over 5000 cycles, which was measured by repeating the GCD test between −0.2 to 0.6 V (*vs.* Ag/AgCl) at a current density of 1 A g^{-1}. Remarkably, only a 12.77% decay in the specific stored charge capacity was observed after 5000 cycles, indicating the remarkable reversibility and stability of the electrode.

4. Conclusions

Graphene/Co_3O_4 nanowire composites with different Co_3O_4 nanowire contents were synthesized *via* a facile three-step synthesis and thermal reduction, and their electrochemical properties were investigated. The Co_3O_4 nanowires were prepared *via* a microemulsion-based method and calcination. The CoC_2O_4 nanowires used as precursors were prepared using the same method. The morphologies of the nanowires were observed *via* FE-SEM. After the ultrasonication and vacuum filtration of a dispersed solution of Co_3O_4 nanowires and GO, 1D Co_3O_4 nanowires were homogeneously distributed between the GO papers. Then graphene/Co_3O_4 nanowire composites were prepared *via* high-temperature reduction, leading to the formation of a layered graphene/Co_3O_4 nanowire hybrid structure. The graphene/Co_3O_4 nanowire composites exhibited high electrical conductivity and a large accessible surface area, resulting in excellent electrochemical performance. Interestingly, the Co_3O_4 content was not directly proportional to the redox reaction. The optimal amount of Co_3O_4 provided the electrolyte easy access to the active material because the Co_3O_4 nanowires affected the spacing of the RGO layers. Excess Co_3O_4 induced aggregation, inhibiting the contact between the activated material and the electrolyte. RGO/Co_3O_4 nanowire sandwiches in the form of papers, with a moderate Co_3O_4 nanowire content of 11.1 wt%, exhibited excellent supercapacitive performance with a specific charge capacity of 278.936 C g^{-1} at a 5 mV s^{-1} scan rate. This performance was mainly due to the synergetic effect between the high electrical conductivity and redox reaction of the Co_3O_4 nanowire. The outstanding electrochemical performance is attributed to the synergistic effect of the optimal-concentration system, wherein the Co_3O_4 nanowires facilitated fast and favorable electrolyte ion diffusion/transport by increasing the *d*-spacing of the graphene film.

Acknowledgements

This research was supported by the Technological Innovation R&D Program (S2335591) funded by the Small and Medium Business Administration (SMBA, Korea) and the Chung-Ang University Graduate Research Scholarship in 2016.

References

1 W. Wei, X. Cui, W. Chen and D. G. Ivey, *Chem. Soc. Rev.*, 2011, **40**, 1697–1721.
2 J. Hansen, M. Sato, R. Ruedy, A. Lacis and V. Oinas, *Proc. Natl. Acad. Sci. U. S. A.*, 2000, **97**, 9875–9880.
3 M. Kim and J. Kim, *ACS Appl. Mater. Interfaces*, 2014, **6**, 9036–9045.
4 Z. Yu, D. Zinger and A. Bose, *J. Power Sources*, 2011, **196**, 2351–2359.
5 Y. Zhu, S. Murali, M. D. Stoller, K. J. Ganesh, W. Cai, P. J. Ferreira, A. Pirkle, R. M. Wallace, K. A. Cychosz, M. Thommes and D. Su, *Science*, 2011, **332**, 1537–1541.
6 M. D. Stoller, S. Park, Y. Zhu, J. An and R. S. Ruoff, *Nano Lett.*, 2008, **8**, 3498–3502.
7 G. Ning, Z. Fan, G. Wang, J. Gao, W. Qian and F. Wei, *Chem. Commun.*, 2011, **47**, 5976–5978.
8 G. D. Lee, C. Z. Wang, E. Yoon, N. M. Hwang, D. Y. Kim and K. M. Ho, *Phys. Rev. Lett.*, 2005, **95**, 205501.
9 T. Brousse, P. L. Taberna, O. Crosnier, R. Dugas, P. Guillemet, Y. Scudeller, Y. Zhou, F. Favier, D. Belanger and P. Simon, *J. Power Sources*, 2007, **173**, 633–641.
10 Y. Lee, J. Jung, S. Park, J. Seo, S. baeck, J. Yoon, J. Yi and I. Song, *Curr. Appl. Phys.*, 2010, **10**, 947–951.
11 K. Xia, Q. Gao, J. Jiang and J. Hu, *Carbon*, 2008, **46**, 1718–1726.
12 T. Kim, G. Jung, S. Yoo, K. Suh and R. Ruoff, *ACS Nano*, 2013, **7**, 6899–6905.
13 D. Wang, F. Li, Z. Chen, G. Lu and H. Cheng, *Chem. Mater.*, 2008, **20**, 7195–7200.
14 Z. Li, Z. Xu, X. Tan, H. Wang, C. H. Holt, T. Stephenson, B. C. Olsen and D. Mitilin, *Energy Environ. Sci.*, 2013, **6**, 871–878.
15 G. Zhu, Z. He, J. Chen, J. Zhao, X. Feng, Y. Ma, Q. Fan, L. Wang and W. Huang, *Nanoscale*, 2014, **6**, 1079–1085.
16 S. Ye, J. Feng and P. Wu, *ACS Appl. Mater. Interfaces*, 2013, **5**, 7122–7129.
17 M. Huang, R. Mi, H. Liu, F. Li, X. Zhao, W. Zhang, S. He and Y. Zhang, *J. Power Sources*, 2014, **269**, 760–767.
18 G. Xu, C. Zheng, Q. Zhang, J. Huang, M. Zhao, J. Nie, X. Wang and F. Wei, *Nano Res.*, 2011, **4**, 870–881.
19 S. Wang and R. Dryfe, *J. Mater. Chem. A*, 2013, **1**, 5279–5283.
20 Z. D. Huang, B. Zhang, R. Liang, Q. B. Zheng, S. Oh, X. Lin, N. Yousefi and J. Kim, *Carbon*, 2012, **50**, 4239–4251.
21 L. Wang, L. Sun, C. Tian, T. Tan, G. Mu, H. Zhang and H. Fu, *RSC Adv.*, 2012, **2**, 8359–8367.
22 S. K. Meher and G. R. Rao, *J. Phys. Chem. C*, 2011, **115**, 15646–15654.
23 C. Yuan, X. Zhang, L. Su, B. Gao and L. Shen, *J. Mater. Chem.*, 2009, **19**, 5772–5777.
24 C. Hu, K. Chang, M. Lin and Y. Wu, *Nano Lett.*, 2006, **6**, 2690–2695.
25 W. S. Hummers Jr and R. E. Offeman, *J. Am. Chem. Soc.*, 1958, **80**, 1339.
26 M. Kim, Y. Hwang and J. Kim, *Phys. Chem. Chem. Phys.*, 2014, **16**, 351–361.
27 X. Dong, X. Wang, J. Wang, H. Song, X. Li, L. Wang, C. Park, C. Ming and P. Chen, *Carbon*, 2012, **50**, 4865–4870.
28 J. Xu, L. Gao, J. Cao, W. Wang and Z. Chen, *Electrochim. Acta*, 2010, **56**, 732–736.
29 M. Kim, I. Oh, H. Ju and J. Kim, *Phys. Chem. Chem. Phys.*, 2016, **18**, 9124–9132.
30 M. Kim, H. Ju and J. Kim, *Phys. Chem. Chem. Phys.*, 2016, **18**, 3331–3338.
31 M. Kim, I. Oh and J. Kim, *Electrochim. Acta*, 2016, **196**, 357–368.
32 T. Bordjiba and D. Belanger, *J. Electrochem. Soc.*, 2009, **156**, A378–A384.